Chapter 4

TRANSIENT EVAPORATION PHENOMENA

4.1 Introduction

The experimental study on highly transient evaporation from a liquid-vapor interface excited by stepwise heating of the interface have been little conducted as mentioned in Sec. 1.2. In the present experiment, the liquid-vapor interface can be stepwise heated by a thermal pulse impingement. In response to the impingement, evaporation starts and the initial equilibrium vapor phase changes to a new vapor state from the interface. The new vapor flow region consists of the Knudsen layer, the uniform flow, contact region and the evaporation wave as depicted in Fig. 4.1. In this Chapter a detailed discussion on the evaporation phenomena in a practically pure system is presented through the comparison of the experimental results with the kinetic theory analysis results.

In the present experiment the time variations of the pressure and the temperature in the vapor phase are measured with a pressure transducer and a superconductive temperature sensor. The propagation speed of the evaporation wave front is also measured with a double probe type superconductive temperature sensor. Also in the He II phase the temperature variation resulting from the impinging and reflected thermal pulses is measured with a superconductive temperature sensor, from which the temperature variation at the free surface can be derived as the boundary

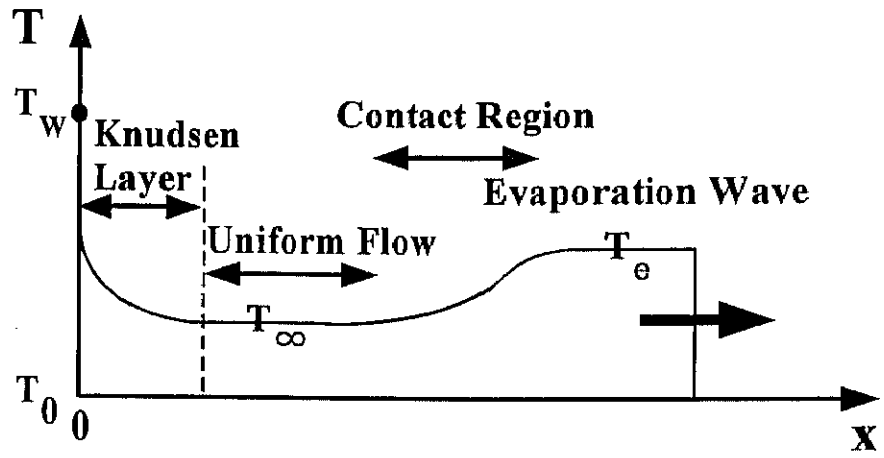

Fig. 4.1: The schematic drawing of the temperature variation in the whole vapor flow region. The x-axis is the distance from a He II free surface. The ordinate is the temperature. T_W; the free surface temperature, T_e; the temperature in the evaporation wave, T_∞; the temperature in the uniform flow region. The whole vapor flow region resulting from transient evaporation consists of the Knudsen layer, a uniform flow, a contact region and an evaporation wave.

condition for evaporation process. In addition to these measurements, the whole evaporation process is visualized with the aid of a laser holographic interferometer.

In this chapter, the experimental results are first discussed. After the kinetic theory analysis for evaporation process is described, the comparison of the experimental result with the kinetic theory analysis result is discussed. Finally, the result of numerical simulation in the vapor flow region is presented.

4.2 Visualization

The interferogram visualization results of evaporation process are shown in Fig. 4.2.b and Fig. 4.3.b, which are finite-fringe mode interferograms, and also in Figs. 4.4.a, b and c, which are infinite-fringe mode interferograms. The formation of a shock is clearly recognized at the evaporation

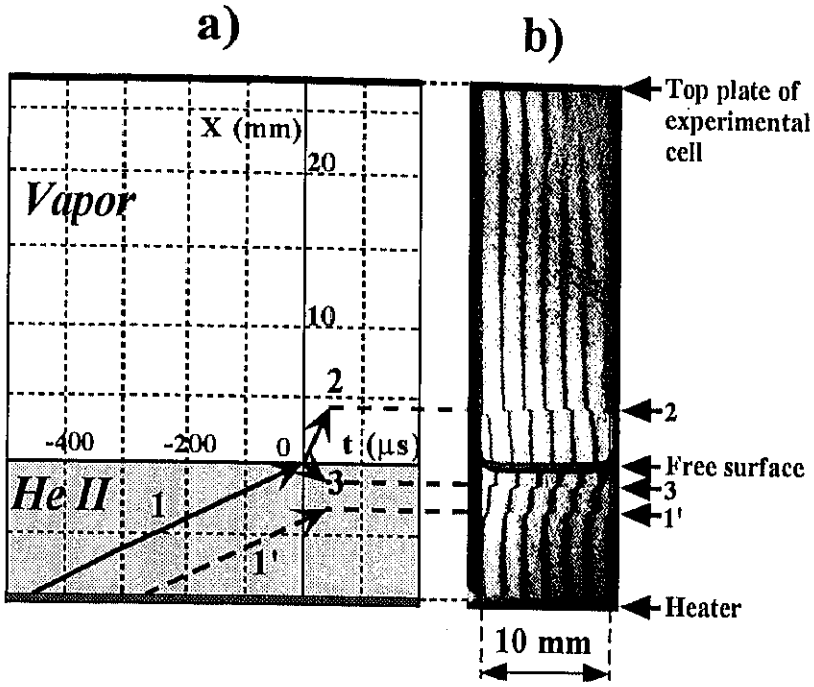

Fig. 4.2: The x-t diagram and the finite-fringe interferogram of the evaporation phenomena. 1: the impinging thermal pulse front, 2: the evaporation wave front, 3: the reflected thermal pulse front, 1′: the impinging thermal pulse tail. a): the x-t diagram for the evaporation phenomena induced by the impingement of a thermal pulse. Solid and broken arrows indicate wave front and tail. b): the finite-fringe interferogram showing the evaporation wave and the thermal pulse. $T_0 = 1.74\,K$, $q = 25\,W/cm^2$, $t_H = 200\,\mu s$, $t_d = 60\,\mu s$, where t_d is the duration time after the thermal pulse incidence onto the free surface to photographing.

wave front in these figures, in which the shock front is indicated by the *arrow* 2. The interferogram shown in Fig. 4.2.b is taken in the finite-fringe mode, in which parallel fringes are intentionally produced in a quiescent state by adjusting an optical element and then they are shifted according to the variation in the refractive index of vapor phase in question. The x-t diagram for the process corresponding to Fig. 4.2.b which was taken at $t_d = 60\,\mu s$ after the thermal pulse incidence onto the free surface is drawn in Fig. 4.2.a, where t_d is the time interval from the thermal pulse incidence onto the free surface to photographing. First a thermal pulse

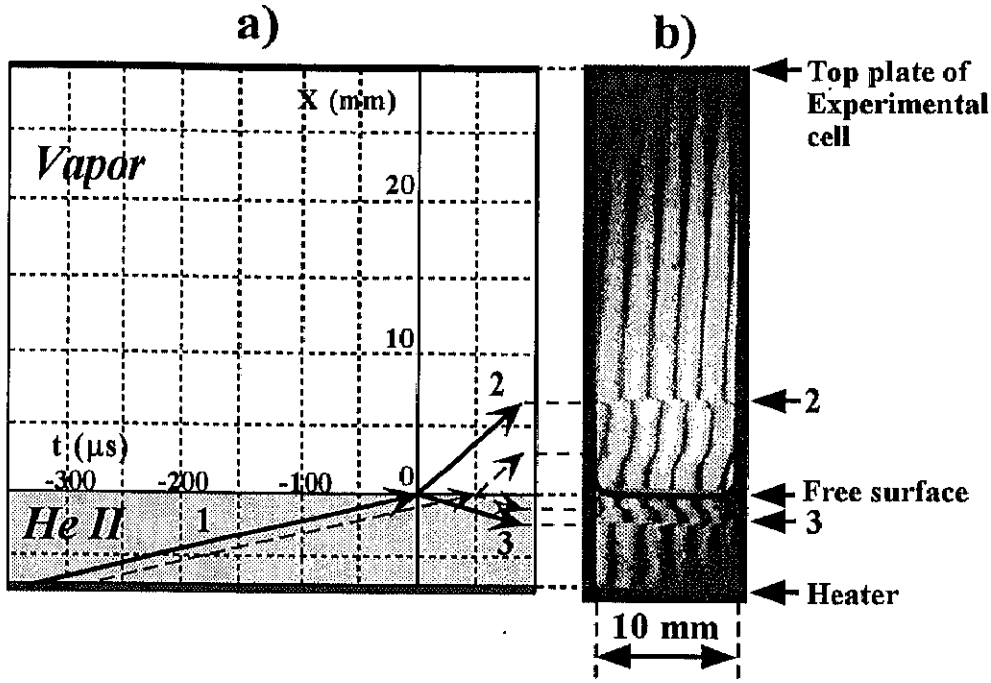

Fig. 4.3: The x-t diagram and the finite-fringe interferogram of the evaporation phenomena. 1: the impinging thermal pulse front, 2: the evaporation wave front, 3: the reflected thermal pulse front. a): the x-t diagram for the evaporation phenomena induced by the impingement of a thermal pulse. Solid and broken arrows indicate wave front and tail. b): the finite-fringe interferogram showing the evaporation wave and the reflected thermal pulse. $T_0 = 1.74\,K$, $q = 40\,W/cm^2$, $t_H = 50\,\mu s$, $t_d = 90\,\mu s$.

emitted from the heater propagates upward through He II nearly at the speed of second sound ($20\,m/s$) as indicated by the *arrow* 1. The impingement of the thermal pulse onto the free surface causes evaporation. An evaporation wave propagates through the vapor phase (*arrow* 2). At the same time, some potion of the impinging thermal pulse is reflected from the free surface propagating downward through He II (*arrow* 3). It is of importance to note that a thermal pulse does not change the sign of the temperature variation upon reflection from a free surface and thus the reflected and impinging thermal pulses overlap each other adjacent to the free surface as indicated in Fig. 4.2.b. The tail of the incident thermal wave resulting from the termination of heating is seen still in He II

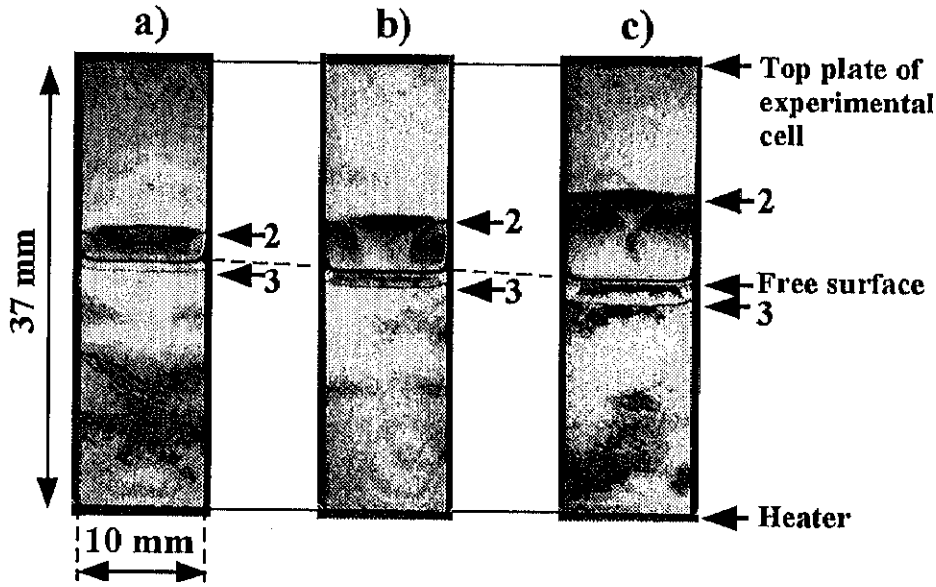

Fig. 4.4: The infinite-fringe interferograms showing the evaporation wave taken at three instances t_d measured from the thermal pulse incidence onto the He II free surface. Evaporation waves from meniscus are recognized. 2: the evaporation wave front and 3: the reflected thermal pulse front. $T_0 = 1.74\,K$, $q = 60\,W/cm^2$, $t_H = 100\,\mu s$. a): $t_d = 40\,\mu s$, b): $t_d = 60\,\mu s$ and c): $t_d = 100\,\mu s$.

as indicated by the *arrow* 1′, but the tail of the evaporation wave is not recognized in the vapor because evaporation still continues at $t_d = 60\,\mu s$. The tails of the evaporation wave in the vapor and of the reflected thermal pulse in the He II are recognized in Fig. 4.3.b. In Figs. 4.4.a, b and c, the evaporation wave fronts (2) and the reflected thermal pulse fronts (3) are seen in the infinite-fringe interferogram. The propagation speed of evaporation wave can also be calculated from these kinds of sequential pictures based on time-of-flight method. It is found that the propagation speed obtained from visualization pictures well agrees with that measured by the double probe superconductive temperature sensor, as described in Sec. 3.1.4. It should be noted that the two fan-shaped evaporation waves seen in Figs. 4.4.a, b and c result from evaporation from the menisci at the free surface-adiabatic wall contact line region. The reflected thermal pulse from the interface propagates downward through He II. In these infinite-

fringe interferograms, the tail of the evaporation wave is not seen because evaporation just finished at $t_d = 100\,\mu s$.

4.3 Temperature Measurement in He II

It is important to measure the temperature variation at the free surface in order to specify the interface boundary condition for evaporation process. For this purpose, the temperature measurement is made in the vicinity of the free surface in He II with a superconductive temperature sensor. Shown in Fig. 4.5 is the time variations of the temperature of impinging and reflected thermal pulses in He II for several values of the heat flux q. It is evident in the data for the case of $q = 10\,W/cm^2$ that the temperature amplitude of the reflected thermal pulse is slightly smaller than that of the impinging one. This temperature decrease results primarily from evaporation. For such a large value of q as $40\,W/cm^2$, the impinging thermal pulse is highly deformed and the peak temperature amplitude is

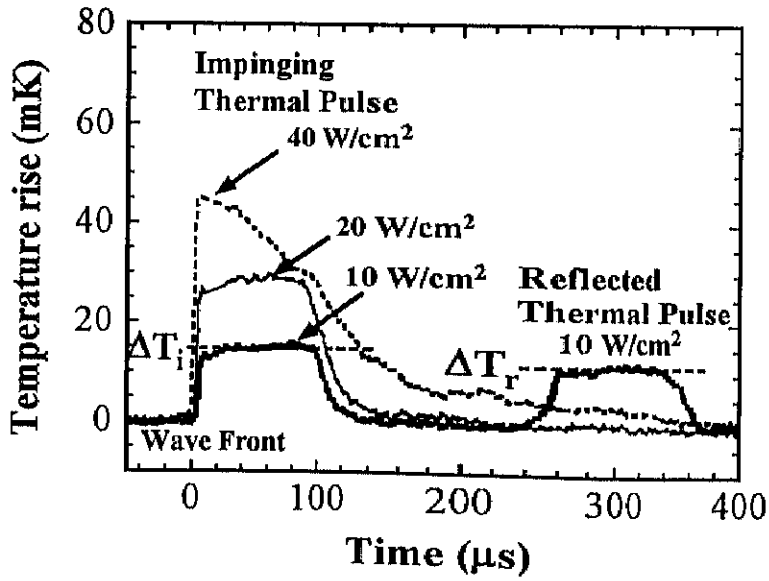

Fig. 4.5: The time variations of the temperature rise of impinging and reflected thermal pulses in He II for several values of q. Reflected thermal pulse is shown only for $10\,W/cm^2$. $T_0 = 1.74\,K$, $t_H = 100\,\mu s$, $q = 10$, 20, and $40\,W/cm^2$.

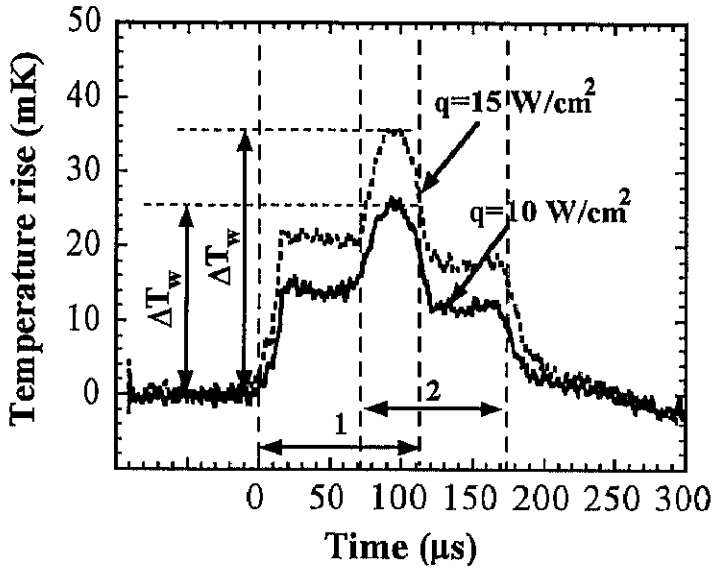

Fig. 4.6: The time variation of the temperature rises resulting from the impinging and the reflected thermal pulses measured adjacent to the He II free surface. The location of the sensor is about 1 mm below the He II free surface. The signal in the overlapped region is a superposition of the impinging thermal pulse indicated by 1 and the reflected thermal pulse by 2. $T_0 = 1.74\,K$, $t_H = 100\,\mu s$, $q = 10$ and $15\,W/cm^2$.

considerably diminished as a result of strong interaction with high density quantized vortices developed in He II under the superfluid breakdown state. Accordingly, the further quantitative studies should be conducted only at smaller q than $20\,W/cm^2$. The free surface temperature rise ΔT_W can be experimentally estimated from the sum of the two temperature rises as

$$\Delta T_W = \Delta T_i + \Delta T_r, \tag{4.1}$$

Here ΔT_i and ΔT_r are the temperature rises of the impinging and reflected thermal pulses measured in He II in the vicinity of a free surface. In Fig. 4.6, the time variations of the temperature rises resulting from impinging and subsequent reflected thermal pulses are presented for two values of q. The reflected and impinging thermal pulses partially overlap with each other like the case shown in the visualization picture, Fig. 4.2.b. It is found that

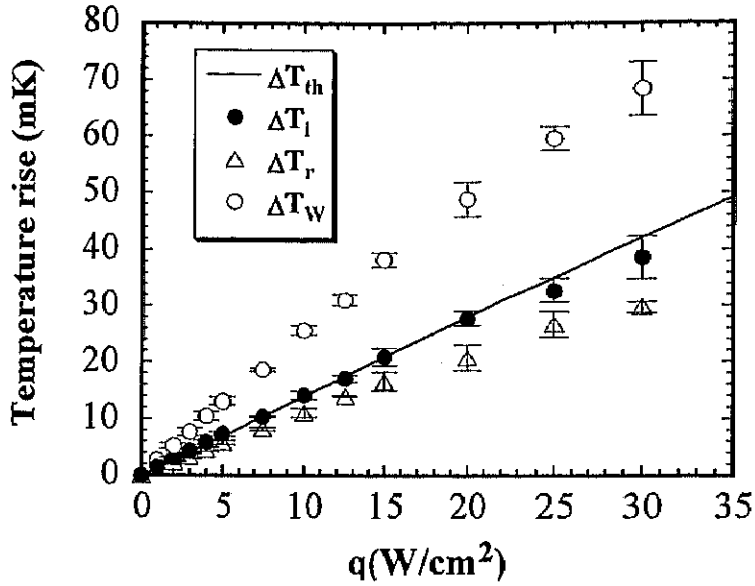

Fig. 4.7: The temperature rises as a function of the heat flux q. $T_0 = 1.74\,K$, $t_H = 100\,\mu s$. ΔT_i, ΔT_r are the experimental results of the temperature rise of the impinging and the reflected thermal pulses, ΔT_W, the experimental result of total temperature rise at the free surface. ΔT_{th}: theoretical temperature rise of an impinging thermal pulse indicated by Eq. (3.1).

the peak value for each case indicated by ΔT_W in the figure is equal to the sum $\Delta T_i + \Delta T_r$ each term of which is measured individually slightly below the free surface. It is, thus, experimentally confirmed that Eq. (4.1) is valid. The relation between the temperature variations, ΔT_i, ΔT_r, and ΔT_W, and the applied heat flux q is plotted in Fig. 4.7. It is seen that the temperature rise ΔT_i slightly deviates from the theoretical value ΔT_{th} given by Eq. (3.1) at large values of q. This must result from the dissipative effect by high density quantized vortices. The same effect is also recognized for other temperature rises, ΔT_r and ΔT_W. In what follows, only data for smaller values of q are used for further discussion.

4.4 Evaporation Wave

The visualization photos of propagating evaporation wave are seen in Sec. 4.2. In this Sec., the pressure and temperature rises in the evaporation wave and the propagation speed of evaporation wave front are quantitatively measured. From the comparison of the experimental result with the Rankin-Hugoniot relation, the shock property of the evaporation wave are discussed.

4.4.1 Pressure measurement

The pressure rise in an evaporation wave is directly measured with the pressure transducer. In every previous study[22][25] of He II evaporation mentioned in the Sec. 1.2 and 1.3, the vapor pressure has never been directly measured, and in stead, it was just estimated from the temperature measurement result on the basis of the assumption that the isoentropic compression can be applied to a weak evaporation wave[25]. Accordingly,

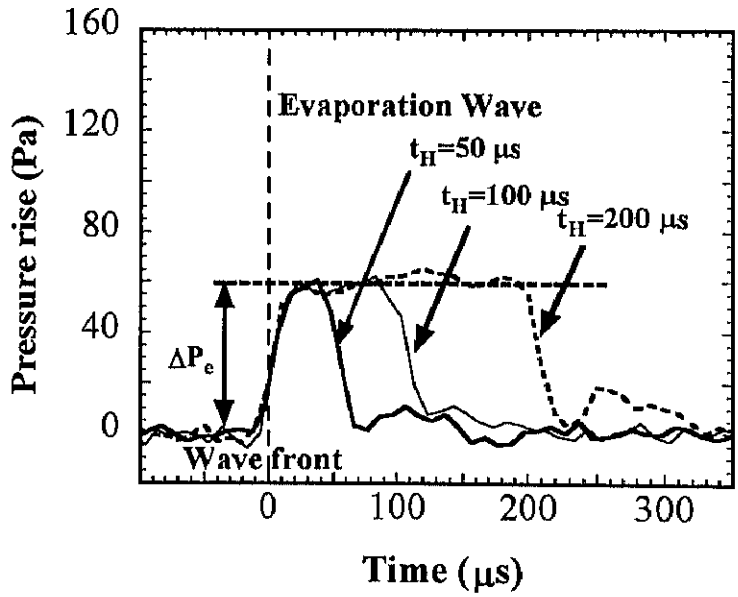

Fig. 4.8: The time variation of the pressure in the evaporation wave. The location of the pressure sensor is about 5 mm above the free surface. $T_0 = 1.74\,K$, $q = 15\,W/cm^2$, $t_H = 50$, 100 and $200\,\mu s$.

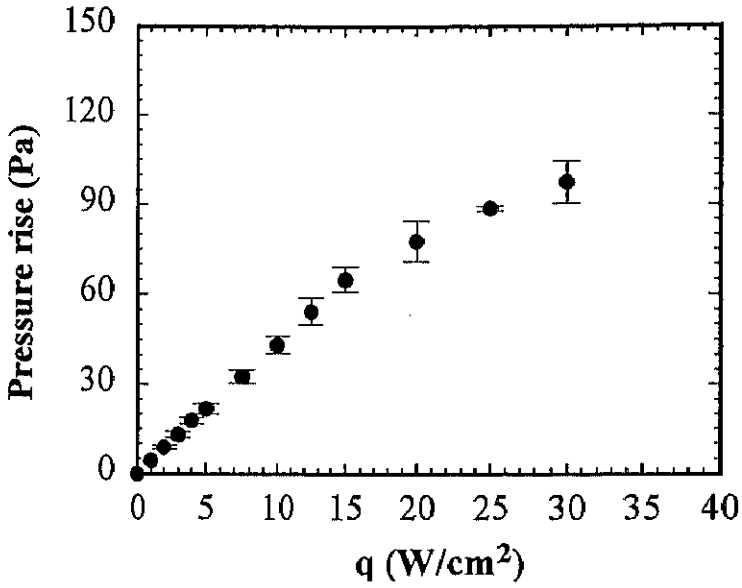

Fig. 4.9: The pressure rise in the evaporation wave as a function of the heat flux q. $T_0 = 1.74$.

it is considered that the pressure values reported in the reference [25] were incorrect because the temperature measurement was incorrect from which the pressure was converted as described in next Sec. The present measurement result of the time variation of the pressure in the evaporation wave is shown in Fig. 4.8 for three cases of the heating time t_H at a heat flux of $15\,W/cm^2$. It is seen from the result that the duration of the pressure rise period well coincides with the heating time. The weak pressure fluctuation with a period of about $70\,\mu s$ is caused by the evaporation waves from the menisci as seen from Figs. 4.4.a, b and c.

The relation between the pressure variation, ΔP_e, and the applied heat flux q is plotted in Fig. 4.9. It is seen that the increasing rate of the pressure rise ΔP_e with q at large values of q becomes smaller than that at small values of q because the impinging thermal pulse is deformed by the dissipative effect of high density quantized vortices for larger values of q as described in Sec. 4.3.

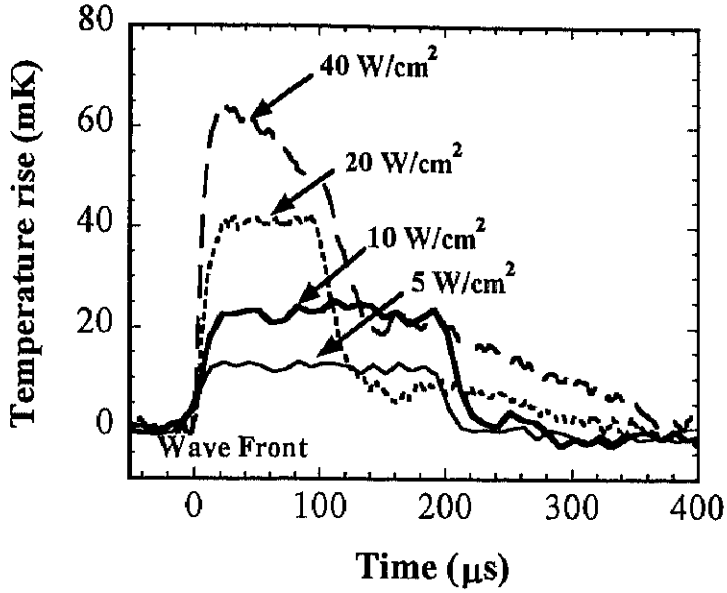

Fig. 4.10: The time variation of the temperature rises in the evaporation wave. $T_0 = 1.74\,K$, $t_H = 200\,\mu s$ for $q = 5$ and $10\,W/cm^2$, and $t_H = 100\,\mu s$ for $q = 20$ and $40\,W/cm^2$.

4.4.2 Temperature measurement

In Fig. 4.10, the time variation data of the temperature rise in an evaporation wave is presented. It is seen that the time variations of the temperature are quite similar to those of the corresponding impinging thermal pulses shown in Fig. 4.5, and that the time duration of every evaporation wave is equal to the heating time of the heater. It should be noted that the temperature drop at the rear of evaporation wave seen in Fig. 4.10 is not caused by the passage of a contact region, but results from the termination of heating from the heater. In the past experimental studies by Kessler and Osborne[22] and Wiechert and Buchholz[25], the temperature in the evaporation wave was measured. But it is now understood that their experiments must have been suffered from some experimental error. Kessler and Osborne[22] indirectly measured it by measuring the sound velocity in an evaporation wave which depends on the temperature. Though this method is, in principle, justified, the effect of fan-shaped evaporation waves resulting from evaporation from menisci as shown in Figs. 4.4.a, b and c would, in

fact, cause serious error in the measurement of sound speed. In the present experiment, the temperature is directly measured near the free surface near the center of the experimental cell, and consequently the meniscus effect can be avoided. Wiechert and Buchholz[25] directly measured the temperature in vapor with an Aluminum film superconducting temperature sensor fixed on the top plate of the experimental cell. However, it is obvious that the sensor film was covered with superfluid thin film in their experimental arrangement. Wiechert and Buchholz[25] supposed that the temperature of the sensing element covered with superfluid thin film become equal to the vapor temperature in the evaporation wave. This supposition is usually wrong because the superfluid thin film on the sensor element is not always in thermal equilibrium in the evaporation wave. Furthermore, since the temperature was measured by the sensor on the top plate of experimental cell, the reflection effect of an evaporation wave on the top plate had to be properly taken into account for the temperature measurement. Wiechert and Buchholz[25] made a rather a priori assumption that the amplitude reflection coefficients of the pressure and the temperature on a superfluid thin film were both 0.7. The correct reflection coefficient on a solid wall covered with superfluid thin film must be almost unity, that is derived on the basis of the normal incident reflection theory supplemented with the Rankine-Hugoniot relation for gas dynamic wave. It is also experimentally confirmed that the correct reflection coefficient is almost unity as will be described in Sec. 7.2. In the present experiment, as described above, the superfluid thin film around the gold-tin superconductive temperature sensor element surface is eliminated by means of self-heating of the element for good thermal coupling of the sensor element with vapor. Of course, as excessively large bias electric current may cause temperature rise of the sensor itself and may heat up the vapor around it through Joule heating, which may result in large error in the measurement, the applied electric current is carefully chosen.

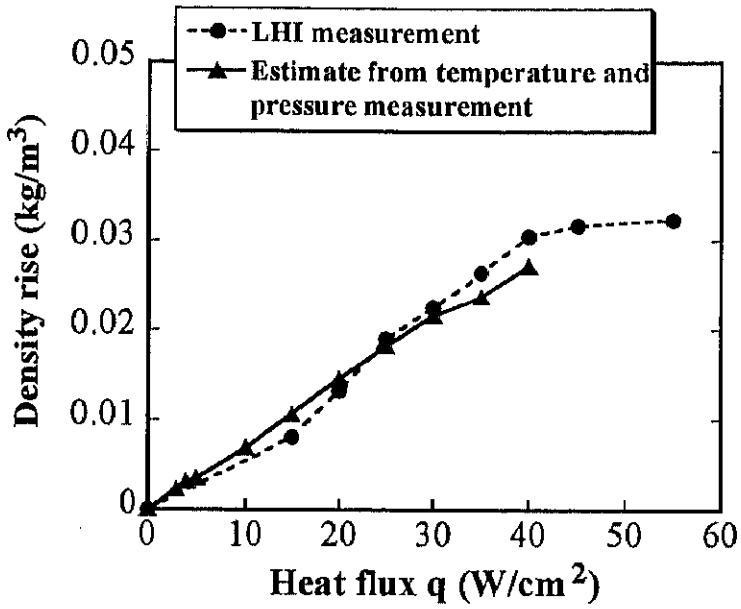

Fig. 4.11: The comparison of the density rise in the evaporation wave measrued with LHI used in the finite-fringe mode with that estimated from the pressure and the temperature measurement data, $T_0 = 1.74\,K$.

4.4.3 Density measurement

As described in Sec. 3.2.1, the density rise in the evaporation wave, $\Delta\rho_e$, can be evaluated from the LHI measurement result by Eq. (3.5). In addition to this, the density rise $\Delta\rho_e$ can also be computed from the temperature and pressure measured in the evaporation wave with the aid of HEPAK. The density rise measurement data through both methods are compared in Fig. 4.11. The agreement is fairy good as a whole. It is demonstrated that the LHI data can be used for the evaluation of the density variation even in relatively low-density vapor in cryogenic environment. It is, however, obvious that there is some systematic discrepancy between both measurement results. The measurement error of LHI becomes larger for lower q, because the magnitude of interference fringe shift is at most 10 % of one interference fringe shift in such cases as $q = 10\,W/cm^2$. Thus the error is estimated to be $\pm 0.003\,kg/m^3$ in this bath temperature range. On the other hand in the cases of higher heat flux q, the discrepancy is

primarily caused by the calibration error of the temperature sensor because the sensor is not well calibrated at higher temperature region.

4.4.4 Rankine-Hugoniot relation

The propagation speed of evaporation wave is measured with the double probe type superconductive temperature sensor. The result is presented in Fig. 4.12 in the form of the shock Mach number, Ms, of evaporation wave, that is defined as the speed ratio of shock wave to sound wave in initial quiescent helium vapor plotted as a function of P_e / P_0 for various cases of the temperature T_0 of initial vapor. Here P_e and P_0 are the pressures of evaporation wave and the saturated vapor pressure at the temperature of T_0. It is seen that the Mach number of propagating evaporation wave is almost unity or slightly larger than unity in every case, and the experimental data are in good agreement with the Rankine-Hugoniot relation[51] indicated by the solid line, which is the general relation among physical

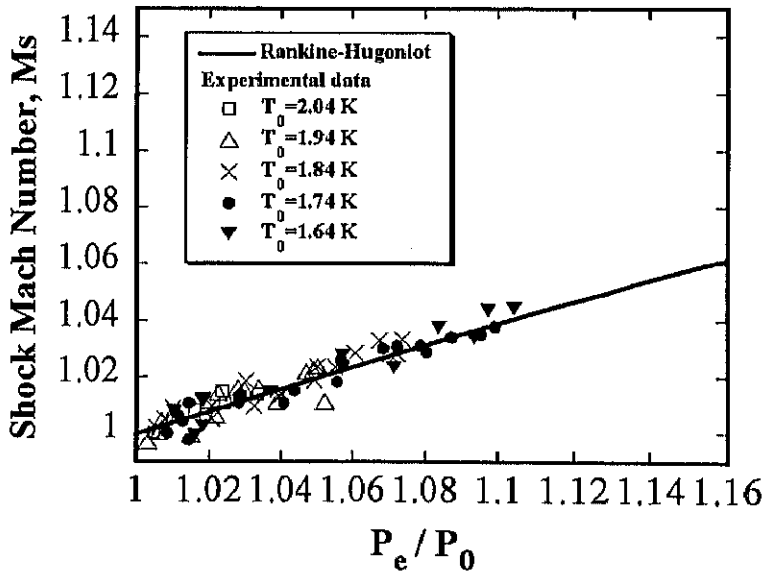

Fig. 4.12: The shock Mach number of evaporation wave, Ms, as a function of P_e/P_0. The solid line indicates the Rankine-Hugoniot relation.

quantities across a shock wave, given by

$$Ms = \sqrt{\frac{\frac{P_e}{P_0} + \mu}{1 + \mu}}, \tag{4.2}$$

where γ and a_0 are the specific heat ratio and the speed of sound in vapor and $\mu = (\gamma - 1)/(\gamma + 1)$. The data scattering results mainly from the measurement error of the time interval between the two signals from the double probe sensor separated by $9.72\,mm$. The response time of each temperature sensor element is a few μs, which may lead to the measurement error of $\Delta(Ms) \simeq 0.01$.

The quantitative measurement of the temperature variation in an evaporation wave can also be made with the double probe temperature sensor. Fig. 4.13 shows the temperature measurement result of T_e normalized by T_0 as a function of P_e / P_0, where T_e is the vapor temperature in the evaporation wave. It is seen that the experimental result also well agrees with the Rankine-Hugoniot relation. From these satisfactory agreements

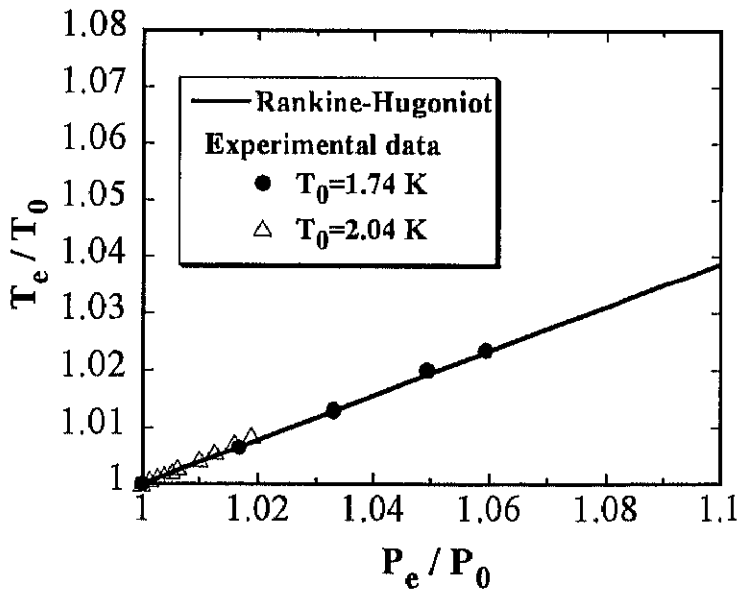

Fig. 4.13: The temperature of evaporation wave, T_e/T_0 as a function of pressure, P_e/P_0 for two cases of the temperature, $T_0 = 1.74$ and $2.04\,K$. The solid line indicates the Rankine-Hugoniot relation between T_e/T_0 and P_e/P_0.

of the experiment data with the Rankine-Hugoniot relations, we may be able to conclude that the temperature and the pressure are adequately measured in the present experiment.

It may be justified from these satisfactory agreements of the experimental results with the Rankine-Hugoniot relation that other physical quantities such as the particle velocity v_e in the evaporation wave that has not yet been measured can be derived from the Rankine-Hugoniot relation provided that the pressure P_e or the temperature T_e is measured. It is, furthermore, known in the kinetic theory of gases that the particle velocity is equal to the vapor flow velocity v_∞ in the uniform flow region, that is very important to investigate the boundary condition at the interface for the evaporation process because the slip boundary condition is given as a function of speed ratio, $v_\infty/\sqrt{2RT_W}$ (or $v_\infty/\sqrt{5/3RT_\infty}$) as described in the next section where T_W and R are the temperature of a free surface and the gas constant.

4.5 Kinetic Theory Analysis for Evaporation Problem

As described in Sec. 1.1, in order to analyze the inside structure of the Knudsen layer, the Boltzmann equation must be solved. The Boltzmann equation is generally presented by

$$\frac{\partial f}{\partial t} + \xi_i \frac{\partial f}{\partial x_i} = J(f, f), \tag{4.3}$$

where ξ_i, f and J are the molecular velocity, the velocity distribution function and the collision integral respectively. The collision integral term is considerably complicate because J is a non-linear differential integral term. Therefore, in order to solve the Boltzmann equation of Eq. (4.3), the collision term of Eq. (4.3) is necessary to be simplified. And the simplified Eq. (4.3) also has the instinct of the collision term. The simplified Boltzmann equation called the BGK model equation is usually analyzed for the kinetic theory analysis of evaporation problem.

In the analysis of the BGK model equation for the evaporation problem, evaporation phenomena should be classified into weak evaporation phenomena and strong evaporation phenomena. The "strong " simply means a high-speed evaporation with shock Mach number of the order of unity. In the analysis of the weak evaporation, the linearized BGK model equation of which the collision term is adequately linearized is solved. On the other hand, in the analysis of strong evaporation, the non-linear BGK model equation is solved. These analytical results of the BGK model equation for the evaporation problem are represented in the form of the slip boundary condition in which the slip quantities, $T_\infty - T_W$ and $P_\infty - P_W$, are given as function of the speed ratio $v_\infty/\sqrt{2RT_W}$ (or $v_\infty/\sqrt{5/3RT_\infty}$). In the present study, the experimental result is compared to the slip boundary conditions in the both cases.

4.5.1 Weak evaporation

The BGK model equation with the linearized the collision term is solved by many authors, for example. The steady-state evaporation problem is solved by Pao[3], Cipolla[4], Sone and Onishi[5][6], Matsushita[8] and so on. The analytical results with different numerical methods are almost same. The analytical solution solved by Sone and Onishi[5] is given for the general case where the effect of the condensation coefficient α_c is taken into account as follows[52],

$$\frac{P_\infty}{P_W} = 1 + \left(C_4^* - 2\sqrt{\pi}\frac{1-\alpha_c}{\alpha_c} \right) \frac{v_\infty}{\sqrt{2RT_W}}, \tag{4.4}$$

$$\frac{T_\infty}{T_W} = 1 + d_4^* \frac{v_\infty}{\sqrt{2RT_W}}, \tag{4.5}$$

where P_W is the saturated vapor pressure at the temperature of T_W. The slip coefficients are $C_4^* = -2.132039$ for the pressure and $d_4^* = -0.446749$ for the temperature. They are, according to Cipolla et al.[4], $C_4^* = -2.1254$ and $d_4^* = -0.4557$, which are almost same as the result by Sone and Onishi[5]. In these derivation, it is assumed that the accommodation coefficient of the free surface which is defined as the degree of the reflection molecules from a

free surface to accommodate to the temperature of the free surface is unity as usually assumed in the kinetic theory approaches. This assumption is generally accepted for cryogenic temperature situations (Brown et al.[53]).

The weakly non-linear BGK model equation for the steady-state evaporation problem is also solved by Onishi and Sone[7]. This analytical result is represented as the same slip boundary conditions of Eqs. (4.4) and (4.5).

4.5.2 Strong evaporation

The non-linear BGK model equation for the transient evaporation problem is solved by Sone and Sugimoto[1] in a pure liquid-vapor system. The quiescent vapor on the liquid phase is compressed by evaporation, and the compression wave propagates upstream infinitely through vapor phase. The vapor flow region behind the wave approaches a steady state as indicated in Fig. 4.1. A steady solution exists when the parameters satisfy the following condition:

$$\frac{P_\infty}{P_W} = \frac{1}{1 + \dfrac{1-\alpha_c}{\alpha_c} K_e(M_{n\infty})} h_1(M_{n\infty}), \tag{4.6}$$

$$\frac{T_\infty}{T_W} = h_2(M_{n\infty}), \tag{4.7}$$

where $M_{n\infty}$ and $K_e(M_{n\infty})$ are defined as

$$M_{n\infty} = \frac{v_\infty}{\sqrt{\frac{5}{3}RT_\infty}}, \tag{4.8}$$

$$K_e(M_{n\infty}) = \sqrt{\frac{10\pi}{3}} \frac{h_1(M_{n\infty})}{\sqrt{h_2(M_{n\infty})}} M_{n\infty}. \tag{4.9}$$

The functions $h_1(M_{n\infty})$ and $h_2(M_{n\infty})$ are presented in Fig. 4.14. The Eqs. (4.6) and (4.7) are the general boundary conditions that the effect of the condensation coefficient α_c is taken into account[52]. It should be noted that the temperature slip condition is unchanged with the inclusion of the condensation coefficient effect.

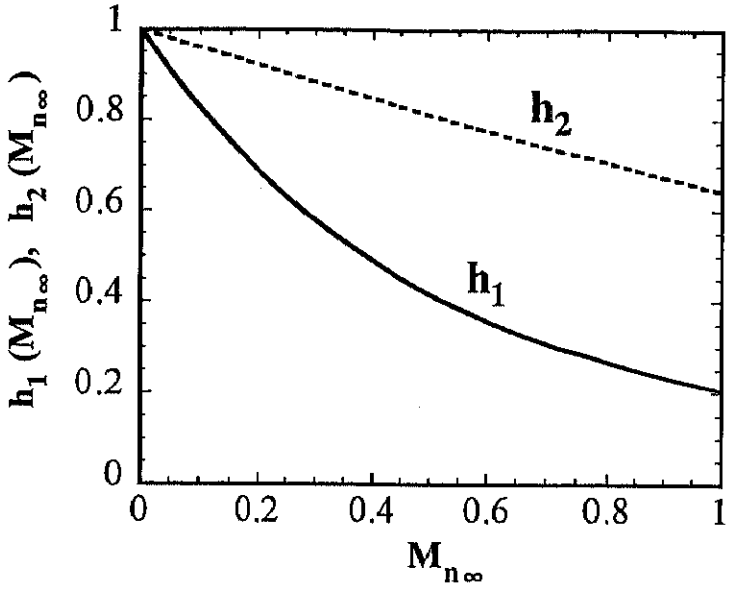

Fig. 4.14: The slip coefficients for the non-linear slip boundary condition, $h_1(M_{n\infty})$ and $h_2(M_{n\infty})$ as a function of $M_{n\infty}$ given in Eqs. (4.6) and (4.7). The solid and broken lines indicate h_1 and h_2.

4.6 Comparison of Experimental Result with Slip Boundary Condition

After a highly transient initial phase of evaporation, a uniform flow region develops between the Knudsen layer and the contact region as described before. In the situation of quasi steady evaporation only the uniform flow region is recognized in the macroscopic vapor field because the evaporation wave propagates far away from the interface and the Knudsen layer is too thin to be recognized. For a physically meaningful comparison of the experimental result with the theoretical one for the slip boundary conditions, Eqs. (4.4), (4.5), (4.6) and (4.7), the temperature T_∞, the pressure P_∞ and the particle velocity v_∞ must be measured in the uniform flow region. However, the direct measurement in the region is very difficult in experiments within such a short heating period as that in the present experiment. The region dose not develop thick enough required for the macroscopic measurement within such a short measurement time as from

the onset of evaporation to the arrival of a reflected evaporation wave from the top plate of the cell at the location of the sensors, because the developing speed of the uniform flow region, or equivalently that of the contact layer behind which the uniform flow region grows, is very small, typically a few m/s. A larger experimental cell with a height large enough to allow longer measuring time within which the uniform region can develop thick, would be a solution to the difficulty. However, long term heating is found to readily cause boiling on the heater, which brings about another experimental difficulty.

In the present experiment, all the physical quantities can not be directly measured inside the uniform flow region. However, the pressure P_∞ and the particle velocity v_∞ in the uniform flow region are available without direct measurements in the region because they are equal to those in

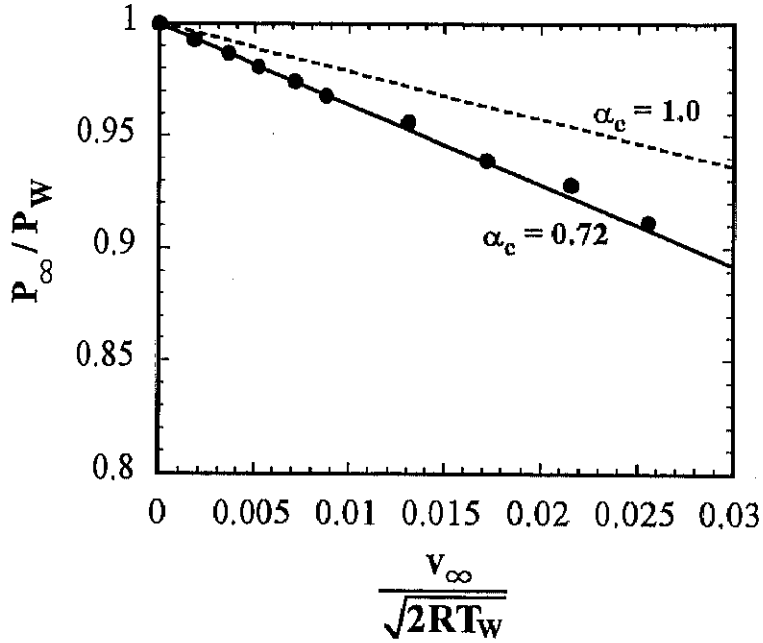

Fig. 4.15: The comparison of the experimental result with the kinetic analysis result with respect to the slip boundary condition at $T_0 = 1.74\,K$. The solid and the broken lines indicate the kinetic analysis results of Eq. (4.4) with $\alpha_c = 0.72$ and 1.0.

the evaporation wave region which can be experimentally measured,

$$P_\infty = P_e, \tag{4.10}$$

$$v_\infty = v_e. \tag{4.11}$$

The particle velocity v_e can be derived from the Rankine-Hugoniot relation with the measurement data of the pressure P_e or the temperature T_e.

In Fig. 4.15, the pressure slip condition is compared between the experimental result and the kinetic theory result, Eq. (4.4). The condensation coefficient α_c is thus obtained to be 0.72 by the method of curve fitting to the experimental data for small $v_\infty/\sqrt{2RT_W}$[54]. The solid line and the broken line indicate the Eq. (4.4) with $\alpha_c = 0.72$ and 1.0. The small discrepancy between the solid line and experimental results as $v_\infty/\sqrt{2RT_W}$ increases may arise from the effect of the non-linearity of the slip boundary condition. This non-linearity of the slip boundary condition will be discussed in next Sec.

4.7 Non-linear Property of Slip Boundary Condition

As the rise of the free surface temperature from the equilibrium state, the non-linear effect the slip boundary condition may arise. The non-linear slip boundary conditions, Eqs. (4.6) and (4.7) are given by solving the non-linear BGK model equation. In order to compare the experimental results with the non-linear slip boundary conditions, the temperature in the uniform flow region must be measured. But in the present experiment, the temperature in the region has not been successfully measured as described before. Here, some attempt to evaluate the non-linear effect of the slip boundary condition is presented in the term of the pressure rise in the evaporation wave. Therefore, the experimental result of the pressure rise in the evaporation wave is compared with the theoretical one taking the temperature rise of the free surface as a parameter. The theoretical pressure rise is estimated as follows[55][56]:

As the slip pressure ratio P_∞/P_W and the slip temperature ratio T_∞/T_W are expressed in terms of the speed ratio $M_{n\infty}$, in Eqs. (4.6) and (4.7),

the relation between T_W and $M_{n\infty}$ must be given. The Rankine-Hugoniot relation for the particle velocity is written as

$$v_e = \frac{(1-\mu)\left(\frac{P_e}{P_0}-1\right)}{\sqrt{(1+\mu)\left(\frac{P_e}{P_0}+\mu\right)}}a_0, \tag{4.12}$$

where a_0 is the speed of sound of the equilibrium quiescent helium vapor. Substituting Eqs. (4.6), (4.10) and (4.11) into Eq. (4.12), Eq. (4.12) is rewritten as

$$v_\infty = \frac{(1-\mu)\left(\frac{P_W}{P_0}\frac{h_1}{1+\frac{1-\alpha_c}{\alpha_c}K_e}-1\right)}{\sqrt{(1+\mu)\left(\frac{P_W}{P_0}\frac{h_1}{1+\frac{1-\alpha_c}{\alpha_c}K_e(M_{n\infty})}+\mu\right)}}a_0, \tag{4.13}$$

where P_W is the saturated vapor pressure at the temperature T_W. The Clausius-Clapeyron relation gives a satisfactory estimation for P_W as,

$$P_W = P_0 \exp\left(\frac{L_0}{RT_0}\frac{\Delta T_W}{T_W}\right), \tag{4.14}$$

where L_0 is the latent heat of evaporation at T_0. Substituting Eq. (4.14) into Eq. (4.13), the following relation among ΔT_W, $M_{n\infty}$ and α_c is given as

$$M_{n\infty}\sqrt{\frac{5}{3}RT_W h_2} - \frac{(1-\mu)\left[\exp\left(\frac{L_0}{RT_0}\frac{\Delta T_W}{T_W}\right)\frac{h_1}{1+\frac{1-\alpha_c}{\alpha_c}K_e}-1\right]}{\sqrt{(1+\mu)\left[\exp\left(\frac{L_0}{RT_0}\frac{\Delta T_W}{T_W}\right)\frac{h_1}{1+\frac{1-\alpha_c}{\alpha_c}K_e}+\mu\right]}}a_0 = 0, \tag{4.15}$$

where $T_W = \Delta T_W + T_0$. For a specified value of α_c, the speed ratio $M_{n\infty}$ is numerically given by solving Eq. (4.15) for ΔT_W. The pressure P_e $(=P_\infty)$

for the case of strong evaporation is given by the substitution of the numerically given values to Eq. (4.6).

In the similar manner, the pressure rise in the evaporation wave for the case of weak evaporation can be derived from Eq. (4.4). In this case, the functional relation between the particle velocity v_∞ and the surface temperature rise ΔT_W has to be given because in Eq. (4.4) the slip pressure ratio P_∞/P_W is expressed in terms of the speed ratio which is given as a function of ΔT_W and v_∞. The relation between T_W and v_∞ can also be given with the aid of the Rankine-Hugoniot relation for the particle velocity in the evaporation wave and Eq. (4.11). The final equation similar to Eq. (4.15) for the case of weak evaporation are found to be

$$v_\infty - \frac{(1-\mu)\left[\exp\left(\frac{L_0}{RT_0}\frac{\Delta T_W}{T_W}\right)\left(1+C_4^{**}\frac{v_\infty}{\sqrt{2RT_W}}\right)-1\right]}{\sqrt{(1+\mu)\left[\exp\left(\frac{L_0}{RT_0}\frac{\Delta T_W}{T_W}\right)\left(1+C_4^{**}\frac{v_\infty}{\sqrt{2RT_W}}\right)+\mu\right]}}a_0 = 0, \quad (4.16)$$

where $C_4^{**} = C_4^* + 2\sqrt{\pi}\frac{1-\alpha_c}{\alpha_c}$. For a specified value of α_c, the speed ratio $M_{n\infty}$ is numerically given by Eq. (4.16) for ΔT_W. The theoretical pressure P_e $(=P_\infty)$ for the weak evaporation process is given by the substitution of this numerically given values into Eq. (4.4).

The comparison of the experimental results and the theoretical pressure rise in the evaporation wave is presented in Figs. 4.16.a and 4.16.b. In Fig. 4.16.a, at $T_0 = 1.74\,K$, the solid lines indicate the theoretical pressure rise results for strong evaporation with $\alpha_c = 0.72$, 0.6 and 1.0, and the dotted line dose the result for weak evaporation with $\alpha_c = 0.72$. In Fig. 4.16.b, at $T_0 = 1.28\,K$, the solid lines indicate the theoretical pressure rise results for strong evaporation with $\alpha_c = 0.77$, 0.6 and 1.0, and the dotted line only indicates the theoretical pressure rise result for weak evaporation with $\alpha_c = 1.0$. In both Figs. 4.16.a and b, the experimental results are indicated by the solid circles. It is found that the experimental results are in good agreement with the theoretical pressure rise results for weak evaporation with $\alpha_c = 0.72$ for $T_0 = 1.74$ or 0.77 for $T_0 = 1.28$ in the cases of small free

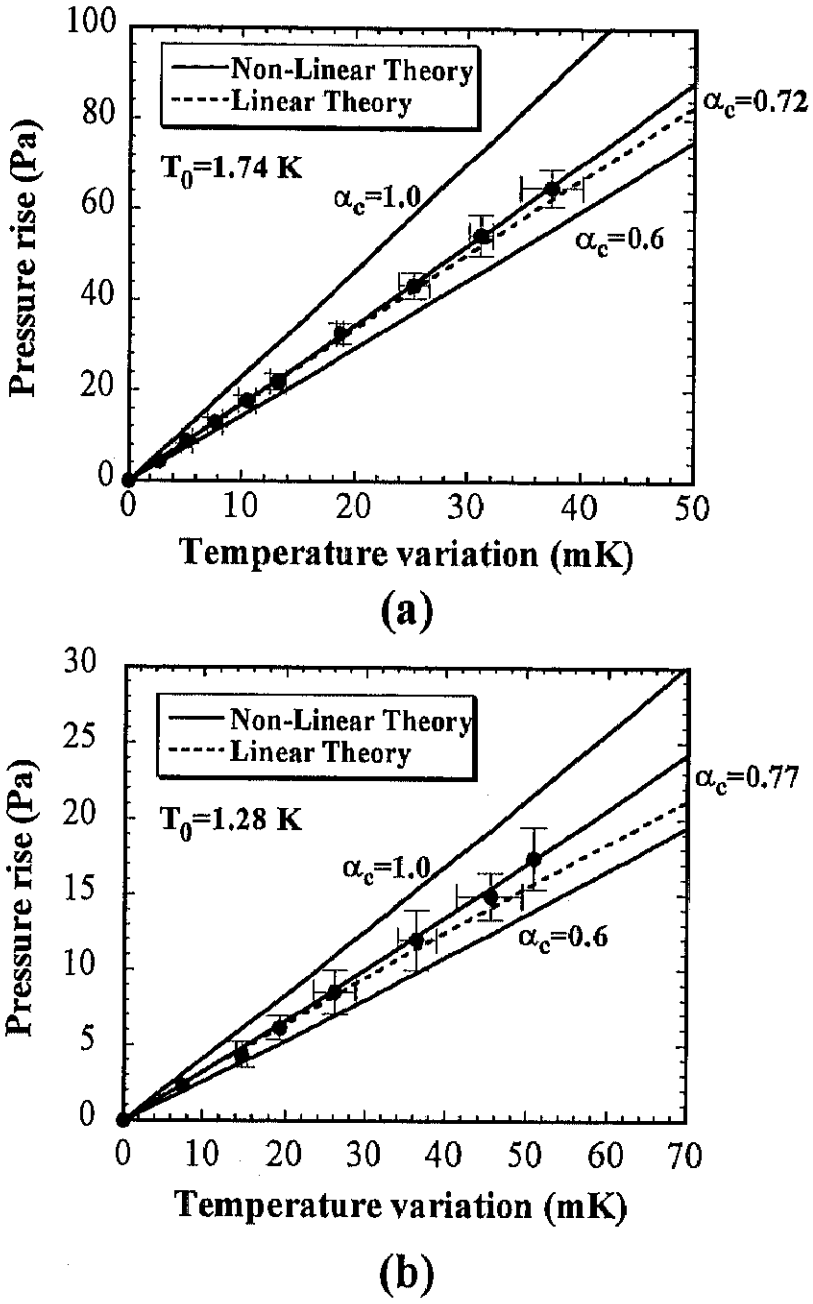

Fig. 4.16: The comparison of the experimental result with the theoretical pressure rise in the evaporation wave. (a): $T_0 = 1.74\,K$, (b): $T_0 = 1.28\,K$. The solid and the broken lines respectively indicate the theoretical pressure rise for strong evaporation and that for weak evaporation.

surface temperature rise. But, as the rise of free surface temperature, the experimental results become to agree rather with the theoretical pressure

rise for strong evaporation. And it is found that the non-linear effect of the slip boundary condition begins to appear at relatively small temperature rise of a free surface.

4.8 Numerical Simulation of Vapor Flow Region

The vapor flow caused by He II evaporation phenomena induced by the stepwise heating on a He II free surface is numerically simulated by solving the one-dimensional Navier-Stokes equation. And the non-linear BGK model equation applied with the boundary condition of stepwise heating on a He II free surface is also solved by Onishi[56][57]. The numerical results solved by Onishi[56][57] are shown in Figs. 4.17.a1 and a2 for the temperature variation and in Figs. 4.17.b1 and b2 for the pressure variation in the case of $T_0 = 1.74\,K$, $q = 10\,W/cm^2$, $\alpha_c = 1.0$. The numerical simulation starts after a He II free surface temperature is changed $\Delta T_W = 25.68\,mK$ from $T_0 = 1.74\,K$. It is found that the evaporation wave is already established at the time of about $50\tau_0 = 17\,ns$, the distance from the free surface to the evaporation wave front is about $50L = 1.41\,\mu m$ and the thickness of Knudsen layer is about $10L = 282\,nm$ at the same time. Here τ_0 is the characteristic time defined by L/a_0, where L and a_0 are the characteristic length defined by $\sqrt{\pi l_0/2}$ and the speed of sound and l_0 is the molecular mean free path. At the temperature $T_0 = 1.74\,K$, τ_0 and L are $339.16\,ps$ and $28.2\,nm$ respectively. It is further found that the Knudsen layer and the contact region are already established at the time of $50\,\tau_0$. But, the uniform flow region is not fully developed even at $134\,\tau_0$. If the numerical simulation is continued far beyond $134\,\tau_0$, the uniform flow region may be developed. In fact this numerical simulation is cost consuming process. Consequently the Navier-Stokes equation is solved with the slip boundary condition in order to analyze the fully developed whole vapor flow region without losing the Knudsen layer effect within a moderate computation time. Fig. 4.18.a and b are the numerical simulation results of the Navier-Stokes equation for the temperature and the pressure variations respectively, $T_0 = 1.74\,K$,

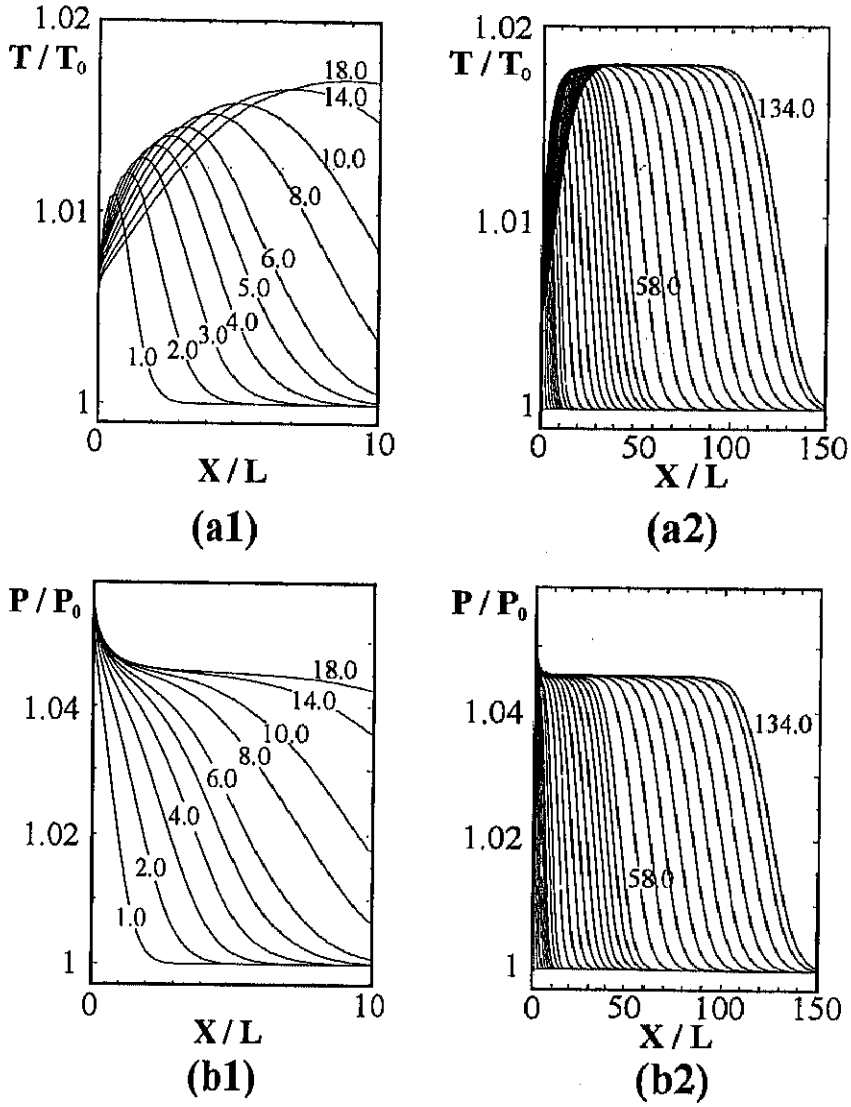

Fig. 4.17: The numerical calculation results of the vapor flow region for He II evaporation solved by Onishi[56][57]. The vapor flow region is numerically calculated by solving the non-linear BGK model equation under the initial condition of stepwise heating, $T_0 = 1.74\,K$, $q = 10\,W/cm^2$, $\alpha_c = 1.0$. L and τ_0 are the characteristic length, $L = 28.2\,nm$ and the characteristic time, $\tau_0 = 339.16\,ps$. (a1) and (a2) for the temperature, (b1) and (b2) for the pressure.

$q = 10\,W/cm^2$, $\alpha_c = 0.72$. The flow field at $t_d = 100\,\mu s$ after the thermal pulse incidence onto He II free surface is drawn. The Navier-Stokes equation is solved with a finite difference computation scheme for the outside

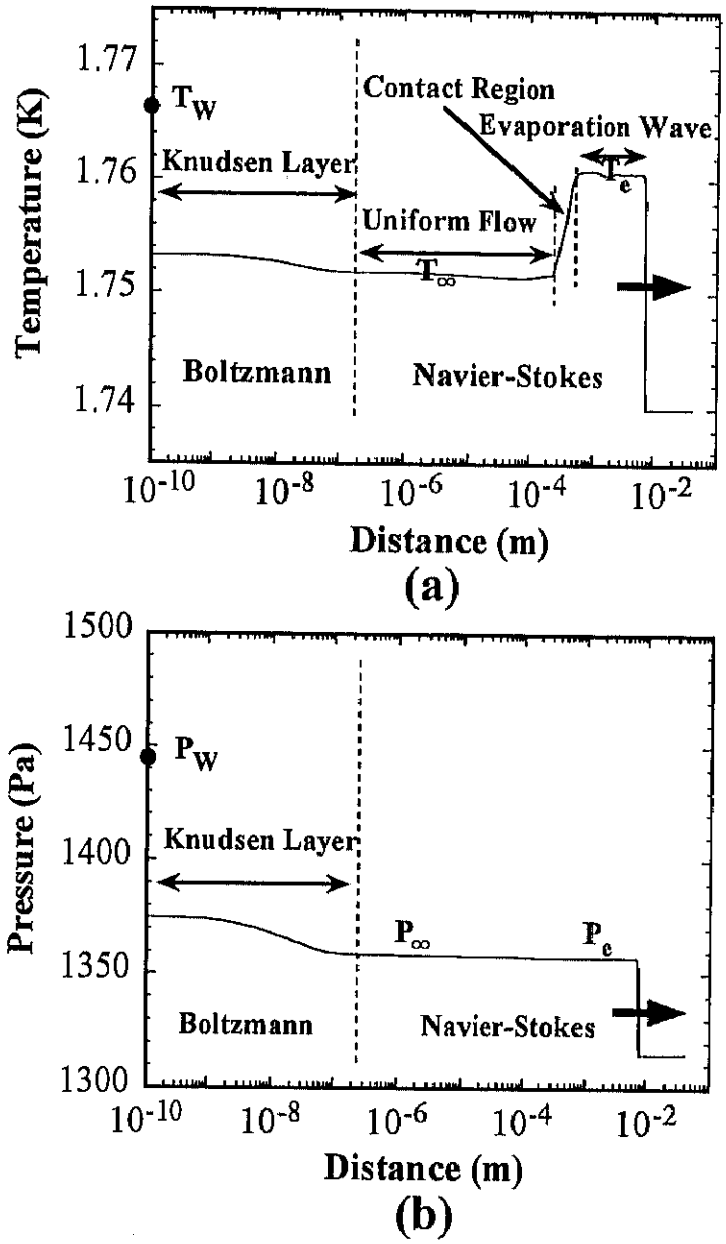

Fig. 4.18: The numerical calculation result of the vapor flow region calculated by solving the Navier-Stokes equation supplemented with the slip boundary condition. $T_0 = 1.74\,K$, $q = 10\,W/cm^2$, $t_d = 100\,\mu s$, $\alpha_c = 0.72$. (a): the temperature, (b): the pressure. The Knudsen function solved by Onishi and Sone[7][52] is presented to illustrate the structure of the Knudsen layer.

region the Knudsen layer. In this study the MacCormack finite difference scheme with flux corrected transport algorithm is adopted to solve the

Navier-Stokes equation. The detail of this numerical scheme is described in Appendix A. On the other hand, for the inside of the Knudsen layer, the analytical result of the BGK model equation is given in the form of the Kundsen functions for the temperature and the pressure variations solved by Onishi and Sone[7], [52]. It is shown in Fig. 4.18.a and b that the whole vapor flow region resulting from transient evaporation consists of the Knudsen layer, the uniform flow region, the contact region and the evaporation wave. As described before, the propagation speed of the contact region is very slow, typically a few m/s, the distance from He II free surface to the contact region is only $0.47\,mm$ at the time $t_d = 100\,\mu s$ and the thickness of the contact region is also $0.23\,mm$ at the same time in the case shown Fig. 4.18.a. And it is confirmed that the experimental result of the pressure and the temperature rises in the evaporation wave is qualitatively in good agreement with the numerical result of these rises.

4.9 Concluding Remarks

The transient evaporation phenomena induced by a thermal pulse impingement onto a He II free surface is experimentally investigated, and following conclusions are drawn.

1. Visualization
   It is demonstrated that a laser holographic interferometer can be applied to the measurement of thermo-fluid dynamic phenomena in He II environment. In the present application to the evaporation process, the propagation of an evaporation wave and a reflected thermal pulse from a free surface are simultaneously seen in a single interferogram.
   (a) It is visualized that a thermal pulse dose not change the sign of the temperature variation upon reflection from a free surface and thus the reflected and impinging thermal pulses overlap each other adjacent to a free surface.
   (b) It is recognized that the formation of a shock is formed at the evaporation wave front.

(c) It is found that the propagation speed obtained from visualization pictures based on time-of-flight method is almost speed of sound in helium vapor.

(d) It is found that the two fan-shaped evaporation wave behind the main evaporation wave result from evaporation from the menisci at the free surface-adiabatic wall contact line region.

2. Temperature measurement in He II

(a) It is experimentally concluded that the free surface temperature rise ΔT_W can be experimentally estimated from the sum of the two temperature rise as $\Delta T_W = \Delta T_i + \Delta T_r$.

(b) It is also found that a thermal pulse dose not change the sign of the temperature variation upon reflection from a free surface and thus the reflected and impinging thermal pulses overlap each other adjacent to a free surface.

3. Evaporation wave

(a) The time variations of the temperature and the pressure in the evaporation wave is measured with a superconductive temperature sensor and a absolute type pressure transducer. It is found that the time variations of temperature and the pressure are quite similar to those of the corresponding impinging thermal pulse.

(b) The propagation speed of evaporation wave is measure with the double probe type superconductive temperature sensor. It is found that the Mach number of propagating evaporation wave is almost unity or slightly larger than unity and the experimental data are in good agreement with the Rankine-Hugoniot relation for a shock Mach number.

(c) It is experimentally confirmed that the experimental results of the temperature and the pressure in the evaporation wave also agree with the Rankie-Hugoniot relation between P_e/P_0 and T_e/T_0.

(d) It is also found that the density rise $\Delta\rho_e$ in the evaporation wave which is obtained with LHI measurement is fairy agree with the density rise that is computed directly from the temperature and the pressure measured in the evaporation wave with the aide of HEPAC.

4. Comparison of the experimental result with the kinetic theory analysis result

   (a) The comparison of the experimental result with the slip boundary condition for linear case

      i. The condensation coefficient α_c is obtained by the method of curve fitting to experimental data for small speed ratio $v_\infty/\sqrt{2RT_W}$.

      ii. It is found at relatively small speed ratio that the small discrepancy between the curve fitting line and experimental results may arise from the effect of non-linearity of the slip boundary condition.

   (b) The effect of non-linearity of the slip boundary condition

      i. The theoretical pressure rise in the evaporation wave as a function a free surface temperature rise ΔT_W is computed from the non-linear slip boundary condition solved by Sone and Sugimoto[1] applied with the Rankine-Hugoniot relation for the particle velocity.

      ii. It is found that the experimental result is good agreement with the theoretical pressure rise in the evaporation wave, and the non-linear effect of the slip boundary condition may arise at relatively small temperature rise of a free surface.

5. Numerical simulation of vapor flow region

   (a) Navier-Stokes equation supplemented with the linear slip boundary condition

i. It is found that the distance from a free surface to the contact region is only $0.47\,mm$ at the time $t_d = 100\,\mu s$, and the thickness of the contact region is also $0.23\,mm$ at the same time.

ii. It is confirmed that the experimental result of the pressure and the temperature rises in the evaporation wave is qualitatively in good agreement with the numerical result of these rises.

(b) Non-linear BGK model equation for He II evaporation solved by Onishi

It is found that the evaporation wave and the Knudsen layer are already established at the time of $17\,ns$ and the thickness of Knudsen layer is only about $282\,nm$ at the same time.